ChemPubSoc Europe

DOI: 10.1002/chem.201703157

CHEMISTRY A European Journal Full Paper

Antitumor Agents

Valproic Acid-Functionalized Cyclometalated Iridium(III) Complexes as Mitochondria-Targeting Anticancer Agents

Rui-Rong Ye, Jian-Jun Cao, Cai-Ping Tan, Liang-Nian Ji, and Zong-Wan Mao*[a]

Abstract: Valproic acid (VPA) is a short-chain, fatty acid type histone deacetylase inhibitor (HDACi), which can cause growth arrest and induce differentiation of transformed cells. Phosphorescent cyclometalated Ir^{III} complexes have emerged as potential anticancer agents. By conjugation of VPA to Ir^{III} complexes through an ester bond, VPA-functionalized cyclometalated iridium(III) complexes **1a**–**3a** were designed and synthesized. These complexes display excellent two-photon properties, which are favorable for live-cell imaging. The ester bonds in **1a**–**3a** can be hydrolyzed quickly by esterase and display similar inhibition of HDAC activity to VPA. Notably, **1a**–**3a** can overcome cisplatin resistance effectively and are about 54.5–89.7 times more cytotoxic than cisplatin against cisplatin-resistant human lung carcinoma (A549R) cells. Mechanistic studies indicate that **1a**–**3a** can penetrate into human cervical carcinoma (HeLa) cells quickly and efficiently, accumulate in mitochondria, and induce a series of cell-death-related events mediated by mitochondria. This study gives insights into the design and anticancer mechanisms of multifunctional anticancer agents.

Introduction

Iridium complexes have recently emerged as promising alternatives to platinum-based metallo-anticancer drugs.[1] Phosphorescent cyclometalated Ir^{III} complexes are regarded as excellent probes for bioimaging and biosensing, due to their outstanding photophysical properties, including relatively high quantum yields, long emission lifetimes, large Stokes shifts, two-photon absorption (TPA) and high photobleaching resistance.[2] On the other hand, cyclometalated Ir^{III} complexes are also considered to be potent anticancer candidates, as they can target subcellular organelles,[3] inhibit protein activities,[4] and act as photodynamic therapeutic agents.[5] We endeavored to develop cyclometalated Ir^{III} complexes as multifunctional theranostic agents integrating anticancer properties and imaging capabilities.[3f,4c,5a,6]

Mitochondria are known as the power houses of a cell, and they also play important roles in many important cellular processes, for example, apoptosis regulation and intracellular signaling.[7] Defects in mitochondrial function are directly related to aging, cancer, and neurodegenerative disorders.[8] With a diverse range of mitochondria-targeted drugs currently in clinical trials, targeting mitochondria as a cancer therapy strategy has had great success in recent years.[9]

Histone deacetylase inhibitors (HDACis) are emerging as a new class of epigenetic anticancer drugs that can promote the acetylation of histones and non-histone proteins and induce transcriptional events involved in growth arrest, differentiation, and apoptotic cell death.[10] With suberoylanilide hydroxamic acid (SAHA) approved by the FDA in 2006 for the treatment of the rare cancer cutaneous T-cell lymphoma, more and more organic-molecule HDACis have been explored for cancer therapy, and several HDACis are now in phase I and II clinical trials.[11] By equipping SAHA with phosphorescent compounds of metals such as ruthenium(II), iridium(III), and rhenium(I), we have developed a series of metal-based HDACis.[4c,12]

Valproic acid (VPA), a clinically used antiepileptic and anticonvulsant drug,[13] has recently been demonstrated as a short-chain, fatty acid type HDACi.[14] Similar to more widely studied HDACis, VPA can cause growth arrest and induce differentiation of transformed cells in culture.[15] Combining VPA with platinum, Shen,[16] Brabec,[18] Gibson[19] and their respective coworkers reported a series of Pt^{IV}-VPA prodrugs, and these complexes exhibited strong synergistic cytotoxicity.

Esterification is an efficient and convenient optimization method for carboxylic acid-containing compounds, which can markedly improve their cellular uptake efficacy.[20] Free VPA hardly enters cells, so that, starting from millimolar concentrations in medium, only low micromolar concentrations were observed in cells.[18] Herein, by conjugating VPA with cyclometalated Ir^{III} complexes through an ester bond, VPA-functionalized Ir^{III} complexes **1a**–**3a** (Scheme 1) were designed and synthesized. Complexes **1b**–**3b**, which lack the VPA group, were used as references. Fluorescence spectroscopy, time-resolved emission spectroscopy, and ESI-MS studies were performed to investigate the hydrolytic process of the ester bonds in **1a**–**3a**. The TPA properties, HDAC inhibitory activities, in vitro

[a] Dr. R.-R. Ye, J.-J. Cao, Dr. C.-P. Tan, Prof. L.-N. Ji, Prof. Z.-W. Mao
MOE Key Laboratory of Bioinorganic and Synthetic Chemistry
School of Chemistry and Chemical Engineering
Sun Yat-Sen University, Guangzhou 510275 (P. R. China)
E-mail: cesmzw@mail.sysu.edu.cn

Supporting information and the ORCID identification number for the author of this article can be found under https://doi.org/10.1002/chem.201703157.

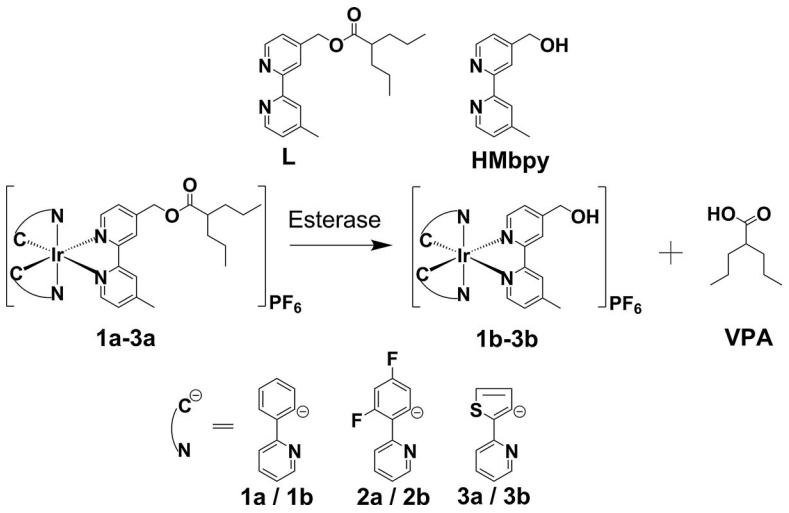

Scheme 1. Chemical structures of ligand **L**, HMbpy, cyclometalated Ir^{III} complexes **1a**–**3a**, and their corresponding hydrolysis products **1b**–**3b** and VPA.

antiproliferative activity, and anticancer mechanisms including subcellular localization, impact on mitochondrial integrity, elevation of reactive oxygen species (ROS), cell-cycle arrest, and induction of apoptosis, were investigated in detail.

Results and Discussion

Synthesis, characterization, and photophysical properties

Ligand **L** was obtained by the reaction of 4-hydroxymethyl-4′-methyl-2,2′-bipyridyl (HMbpy) with 2-propylvaleryl chloride for 12 h at room temperature. Complexes **1a**–**3a** and **1b**–**3b** were synthesized by heating two equivalents of **L** or HMbpy with the corresponding Ir^{III} chlorido-bridged dimer in refluxing CH_2Cl_2/CH_3OH under nitrogen for 4 h. The synthetic routes to ligand **L**, **1a**–**3a**, and **1b**–**3b** are shown in Schemes S1–S3 of the Supporting Information. Complexes **1a**–**3a** and **1b**–**3b** were characterized by ESI-MS, ^1H and ^{13}C NMR spectroscopy (Figures S1–S12 of the Supporting Information), and elemental analysis. The structures of **2a** and **2b** were also determined by X-ray diffraction (Figure 1). The crystal data and selected bond lengths and angles are listed in Tables S1 and S2 of the Supporting Information.

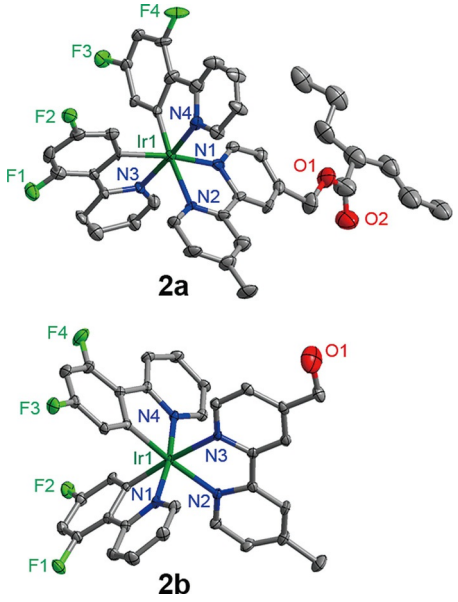

Figure 1. X-ray crystal structures of **2a** and **2b**. The hydrogen atoms and counterions are omitted for clarity.

The photophysical properties of the Ir^{III} complexes were investigated in phosphate buffered saline (PBS), CH_2Cl_2, and CH_3CN. They all show intense absorption bands at 250–450 nm (Figure S13A of the Supporting Information), which can be assigned to mixed ligand-centered (LC) transition, ligand-to-ligand charge transfer, and singlet and triplex metal-to-ligand charge transfer (^{1}MLCT and ^{3}MLCT). On excitation at 405 nm, **1a**–**3a** and **1b**–**3b** exhibit green to red phosphorescent emissions (Figure S13B of the Supporting Information). Quantum yields of the Ir^{III} complexes range from 0.002 to 0.29, and phosphorescence lifetimes lie between 18.60 and 951.56 ns in different solvents at room temperature (Table S3 of the Supporting Information). Compared with reference complexes **1b**–**3b**, conjugation of VPA to Ir^{III} complexes can increase the emission lifetimes of conjugates **1a**–**3a** in PBS. As shown in Table S3 of the Supporting Information, the emission lifetimes of **1a**–**3a** in PBS are increased approximately 6.7-, 2.5-, and 17.6-fold compared with those of **1b**–**3b**, respectively. Moreover, the emission spectra of **1a**–**3a** also show redshifts, due to the electron-donating $OCH(CH_2CH_2CH_3)_2$ group of VPA. For complexes with the same $\widehat{CN}$ ligand, the energy gap between the HOMO and the LUMO can be decreased by increasing the conjugated length of $\widehat{NN}$ ligands, which elicits a redshift of the emission wavelength and an increase in emission lifetime.[21]

Two-photon absorption (TPA) cross sections

Cyclometalated iridium(III) complexes are good candidates for two-photon phosphorescent imaging.[2b,3f] Their two-photon excitation has several advantages over conventional

one-photon excitation, such as decreased photobleaching effects, minimal photodamage to cellular structures, low background interference, and deep penetration.[22] The TPA properties of **1a–3a** and **1b–3b** were investigated by using a two-photon-induced fluorescence method with rhodamine B as a reference in CH_3OH, and the cross sections were determined in the wavelength range of 720–890 nm. Over the measured range, the maximum TPA cross sections δ_{max} of **1a–3a** and **1b–3b** ranged from 38 to 129 GM (1 GM = 10^{-50} cm^4 photon^{-1}) at $\lambda = 740$ nm (Figure S14 and Table S3 of the Supporting Information). These values are moderate compared with those of other Ir^{III} complexes measured by the same method.[5b,c,23] From the log–log plot of the emission intensity against incident power, the linear regression slopes of **1a–3a** and **1b–3b** are 1.98±0.01, 2.00±0.03, 2.05±0.01, 1.95±0.02, 2.05±0.01 and 1.94±0.01, respectively, which indicate nonlinear TPA of the Ir^{III} complexes (Figure S15 of the Supporting Information).

Hydrolysis by esterase in vitro

Ester-modified compounds have been widely used as prodrugs. They can be hydrolyzed selectively or nonselectively by a variety of esterases to release active pharmacophores.[24] The responses of **1a–3a** to esterase were monitored by fluorescence spectroscopy, time-resolved emission spectroscopy,[25] and ESI-MS.[26] Herein, porcine liver esterase (PLE) was used as a model to investigate the hydrolytic process of the ester bonds in **1a–3a**. Time-dependent emission studies showed that the ^{3}MLCT emissions of **1a–3a** show a decrease in intensity on treatment with PLE for 1 h (Figure 2A). The emission intensities decreased by a factor of about 3.4, 2.9, and 11.4 for **1a–3a**, respectively. The hydrolytic half-lives of **1a–3a** are 14.5, 12.7, and 7.3 min, respectively. No significant changes in the emission of **1b–3b** were found on treatment with PLE for the same time (Figure S16 of the Supporting Information), which indicates that the observed emission decrease of **1a–3a** is a result of the release of VPA after hydrolysis by esterase.

Time-resolved emission decay was also used to investigate the hydrolytic process of the ester bonds in **1a–3a**. As shown in Figure 2B, the emission decay curves of **1a–3a** treated with PLE for different time intervals gradually approach that of reference complexes **1b–3b**, respectively. The luminescence lifetimes are 326.75 and 48.61 ns for **1a** and **1b**, respectively. On treatment of **1a** with PLE for 10, 30, and 60 min, the luminescence lifetimes of the system were 218.38, 177.50, and 74.95 ns, respectively (Figure 2Ba). The decreased lifetimes are probably due to hydrolysis of the ester linkage. Similar results were also obtained after incubation of **2a** or **3a** with PLE for different time intervals (Figure 2Bb and c).

Equal amounts of **1a–3a** were incubated with PLE in PBS for different time intervals. The mass spectra of **1a–3a** showed peaks assigned to intact complexes as well as peaks corresponding to reference complexes (Figure S17–S19 of the Supporting Information). The results indicate that **1a–3a** can undergo hydrolysis in the presence of esterase.

HDAC enzyme inhibition assay

The HDAC inhibitory activities of VPA, **1a–3a**, and **1b–3b** were measured by using a commercially available HDAC assay kit, and the results are summarized in Figure 3. In the present study, we found that 1 mM VPA could inhibit 59% of the

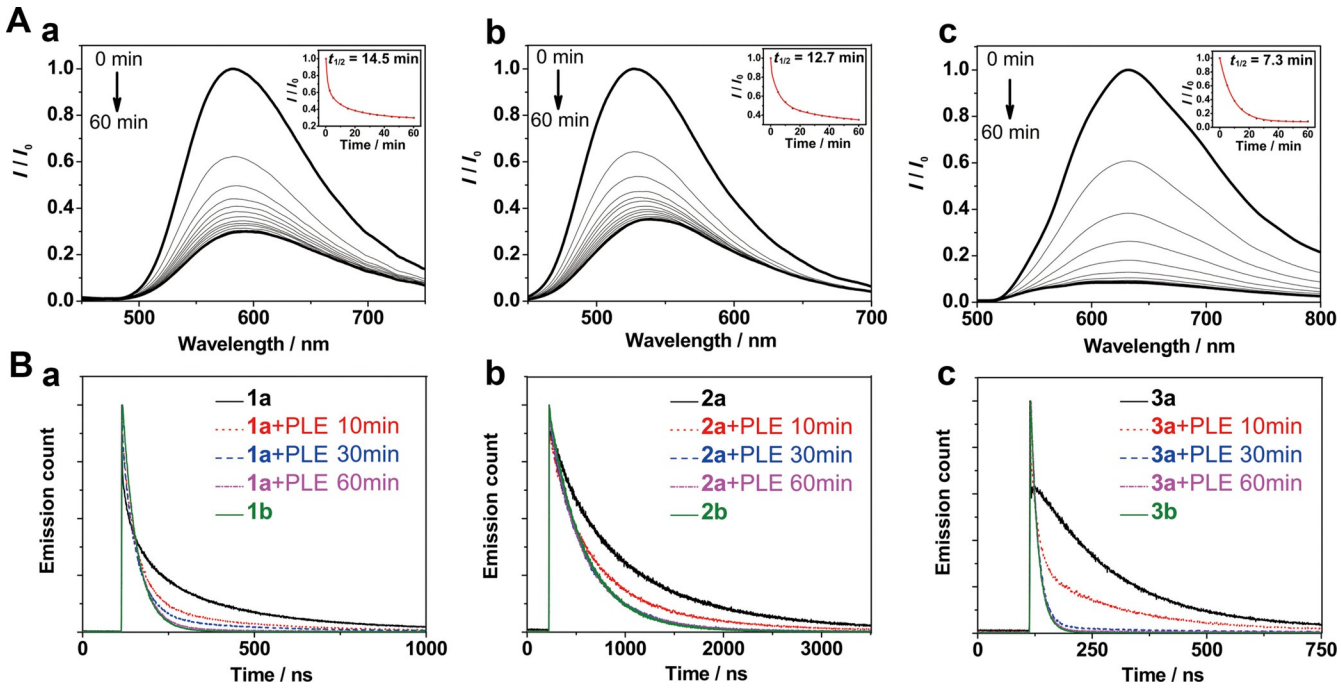

Figure 2. A) Time-dependent changes in emission spectra (2×10^{-5} M, λ_{ex} = 405 nm) of **1a** (a), **2a** (b), and **3a** (c) with PLE at 298 K; insets: plots of relative emission intensities at 584 nm (**1a**), 527 nm (**2a**), and 631 nm (**3a**) versus time of esterase treatment. B) Time-resolved emission decay curves of **1a** (a), **2a** (b), and **3a** (c) on treatment with PLE at 298 K for different time intervals, which were compared with those of **1b**, **2b** and **3b**, respectively.

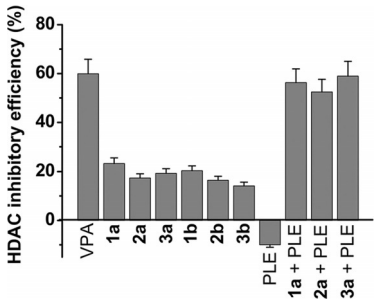

Figure 3. HDAC inhibition activity of VPA, **1a–3a**, **1b–3b**, PLE, and mixtures of **1a–3a** with PLE. Data are shown as mean ± SD of three independent experiments.

HDAC activity. Complexes **1a–3a** and **1b–3b** at 1 mM VPA-equivalent dose showed 23, 17, 19, 20, 16, and 14% inhibition of the HDAC activity, respectively. When **1a–3a** were pretreated with PLE at 298 K for 10 h, their HDAC inhibitory activity dramatically increased to 56, 52, and 59%, respectively. This indicates that once the ester bonds in **1a–3a** are hydrolyzed, free VPA is released, the VPA effectively elicits HDAC inhibition activity, and the produced **1b–3b** do not interfere with HDAC inhibition by VPA.

Lipophilicity and cellular uptake efficacy of Ir^{III} complexes

Lipophilicity lg*P* can strongly influence the cellular uptake, localization, and cytotoxicity of a compound.[27] The lipophilicity of **1a–3a** and **1b–3b** was determined by the flask-shaking method. The lg*P* values obtained for the compounds are in the following order: **2a** (2.9) > **1a** (2.1) > **3a** (2.0) > **2b** (1.8) > **1b** (1.0) > **3b** (0.9) (Table S4 of the Supporting Information). The result indicates that the conjugation of VPA to Ir^{III} complexes can enhance the lipophilicity of **1a–3a**.

As iridium is an exogenous element, the quantitative measurement of the cellular uptake levels of **1a–3a** and **1b–3b** was determined by inductively coupled plasma mass spectrometry (ICP-MS). On incubation of 5 μM complexes with human cervical carcinoma (HeLa) cells for 30 min, the intracellular iridium contents of compounds were in the following order (Table S4 of the Supporting Information): **2a** (1174.7(± 100.5) ng per 10^6 cells) > **1a** (610.0(± 59.2) ng per 10^6 cells) > **3a** (578.4(± 46.8) ng per 10^6 cells) > **2b** (564.2(± 50.0) ng per 10^6 cells) > **1b** (434.2(± 48.2) ng per 10^6 cells) > **3b** (361.0(± 35.1) ng per 10^6 cells). The cellular uptake efficiency of **1a–3a** and **1b–3b** is well correlated with their lipophilicity.

In vitro cytotoxicity

The cytotoxicities of VPA, **1a–3a**, **1b–3b**, and the mixtures of **1b–3b** with VPA (**1b** + VPA, **2b** + VPA, and **3b** + VPA) were determined by 3-(4,5-dimethylthiazol-2-yl)-2,5-diphenyltetrazolium bromide (MTT) assay against HeLa, human pulmonary carcinoma (A549), cisplatin-resistant A549 (A549R), human hepatocellular liver carcinoma (HepG2), and human normal liver (LO2) cells. On the basis of the IC_{50} values (Table 1), the in vitro antiproliferative efficacies of the compounds are in the following order: **1a**, **2a**, **3a** > **1b**, **2b**, **3b** ≈ **1b** + VPA, **2b** + VPA, **3b** + VPA > cisplatin > VPA. VPA (IC_{50} > 100 μM) is inactive against all the cell lines tested. This is in agreement with the above HDAC inhibition results and reports in literature that VPA needs millimolar doses to elicit HDAC inhibition and cytotoxicity.[15,28]

Table 1. IC_{50} values of tested compounds towards different cell lines.[a]

Compound	IC_{50} [μM]				
	HeLa	A549	A549R	HepG2	LO2
1a	0.54 ± 0.05	2.0 ± 0.2	1.0 ± 0.1	0.62 ± 0.06	4.1 ± 0.4
2a	0.48 ± 0.04	1.9 ± 0.2	0.79 ± 0.06	0.75 ± 0.05	3.3 ± 0.3
3a	0.64 ± 0.05	1.7 ± 0.1	1.3 ± 0.1	0.92 ± 0.08	3.8 ± 0.3
1b	2.1 ± 0.2	13.8 ± 1.1	8.2 ± 0.7	3.6 ± 0.3	17.8 ± 1.7
2b	1.5 ± 0.1	10.4 ± 1.0	5.6 ± 0.5	2.2 ± 0.2	13.1 ± 1.3
3b	2.2 ± 0.2	14.7 ± 1.0	10.9 ± 1.0	3.5 ± 0.3	16.2 ± 1.5
1b + VPA	2.6 ± 0.2	12.5 ± 1.2	8.5 ± 0.8	3.4 ± 0.4	18.0 ± 1.8
2b + VPA	1.4 ± 0.1	9.8 ± 1.0	6.0 ± 0.6	2.8 ± 0.2	13.5 ± 1.3
3b + VPA	2.8 ± 0.2	15.2 ± 1.5	10.0 ± 1.0	3.5 ± 0.4	17.6 ± 1.7
VPA	> 100	> 100	> 100	> 100	> 100
cisplatin	23.5 ± 2.3	20.6 ± 2.1	70.9 ± 7.1	20.5 ± 2.1	30.8 ± 2.9

[a] Data are presented as mean ± SD, and cell viability was assessed after 48 h of incubation.

Conjugates **1a–3a**, which have IC_{50} values ranging from 0.48–2.0 μM, show higher cytotoxicity than the other compounds screened against all of the human cancer cells. Specifically, **1a** (IC_{50} = 1.0 μM), **2a** (IC_{50} = 0.79 μM), and **3a** (IC_{50} = 1.3 μM) are approximately 70.9, 89.7, and 54.5 times more potent than cisplatin (IC_{50} = 70.9 μM) against A549R cells, respectively, and thus these complexes can overcome cisplatin resistance. Furthermore, they exhibit a certain selectivity toward human cancer cells over noncancerous cells, as **1a–3a** show 6.6, 4.4, and 4.1 times lower cytotoxicity against LO2 cells than against HepG2 cells, respectively. Reference complexes **1b–3b** show much higher cytotoxicity than VPA and cisplatin, with IC_{50} values ranging from 1.5 to 14.7 μM. The mixtures of **1b–3b** with free VPA (**1b** + VPA, **2b** + VPA, and **3b** + VPA) show comparable cytotoxicity to **1b–3b**, that is, simply mixing them does not improve the antiproliferative efficacy. Moreover, conjugation of the VPA to the Ir^{III} complexes can enhance their anticancer potency; **1a–3a** are about 2.9–8.9 times more cytotoxic than **1b–3b** or their simple mixtures with VPA against all of the human cancer cells.

Cellular localization and uptake mechanisms of Ir^{III} complexes

Studies on cellular localization of phosphorescent metal complexes can provide further clues for the investigations of anticancer mechanisms.[27] By taking advantage of the rich photophysical properties of cyclometalated Ir^{III} complexes, the intracellular distribution of **1a–3a** was investigated by one-photon microscopy (OPM) and two-photon microscopy (TPM) confocal luminescence imaging. As shown in Figure 4, all Ir^{III} complexes can be effectively taken up by HeLa cells and exhibit obvious organelle accumulation after 30 min incubation. Co-localization experiments on **1a–3a** with commercial MitoTracker Deep Red

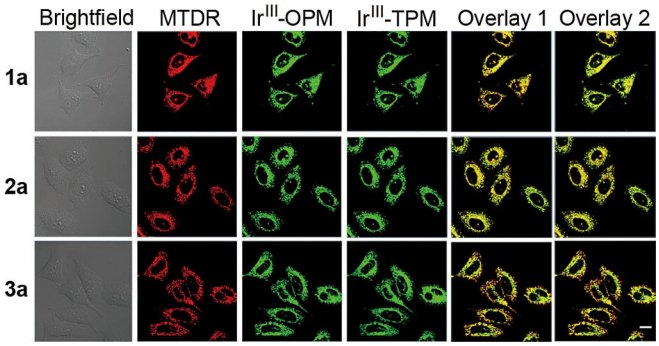

Figure 4. OPM and TPM images of HeLa cells co-labeled with Ir^{III} complexes (5 μM, 30 min) and MTDR (150 nM, 30 min). Complexes **1a**–**3a** were excited at 405 nm (OPM) or 740 nm (TPM). MTDR was excited at 633 nm. The phosphorescence/fluorescence was collected at 600(±20) nm for **1a**, 530(±20) nm for **2a**, 630(±20) nm for **3a**, and 665(±20) nm for MTDR. Overlay 1: overlay of the 2nd and 3rd columns. Overlay 2: overlay of the 2nd and 4th columns. Scale bar: 20 μm.

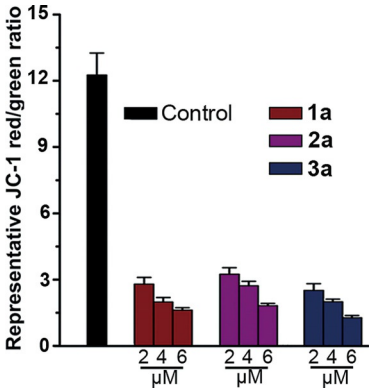

Figure 5. Representative JC-1 red/green ratio obtained from three independent experiments. Data are shown as mean ± SD of three independent experiments.

FM (MTDR) under one- and two-photon excitation demonstrate specific mitochondrial staining of the complexes. Under two-photon excitation, the Pearson's correlation coefficients of **1a**–**3a** with MTDR are all greater than 0.85. Meanwhile, negligible co-localization for **1a**–**3a** with LysoTracker Deep Red FM (LTDR) was observed (Figure S20 of the Supporting Information), which indicates that **1a**–**3a** can specifically label mitochondria.

We further investigated the cellular uptake mechanisms of **1a**–**3a**. Incubation of HeLa cells with **1a**–**3a** at 4 °C or on pretreatment with the metabolic inhibitor carbonyl cyanide 3-chloro-phenylhydrazone (CCCP) leads to reduced cellular uptake efficiency (Figure S21–S23 of the Supporting Information). However, no obvious alteration of the uptake level of **1a**–**3a** is observed in cells pretreated with chloroquine, which modulates endocytosis by inhibiting the acidification of endosomes. The results indicate that the cellular uptake of **1a**–**3a** was mainly through an energy-dependent mechanism, which is similar to other cyclometalated Ir^{III} complexes previously reported.[3e, 5a, 6b]

Impact on mitochondrial membrane potential (MMP)

As **1a**–**3a** could localized to mitochondria, their impact on mitochondrial integrity was monitored by flow cytometry. The changes in MMP were detected by 5,5′,6,6′-tetrachloro-1,1′-3,3′-tetraethyl-benzimidazolylcarbocyanine iodide (JC-1) staining. Mitochondrial depolarization is indicated by a decrease in the red/green fluorescence intensity ratio.[29] As shown in Figure S24 of the Supporting Information, compared with the vehicle-treated cells, cells treated with **1a**–**3a** cause a marked red-to-green color shift, indicating the loss of MMP. Representative JC-1 red/green ratio signals are shown in Figure 5; cells treated with **1a**–**3a** for 6 h show a concentration-dependent decrease in JC-1 red/green fluorescence ratios. Notably, treatment of HeLa cells with **1a**–**3a** (6 μM) at concentrations of approximately 10 times the IC_{50} values significantly decreased the JC-1 red/green fluorescence ratios (control: 12.2 ± 1.0; **1a**: 1.6 ± 0.1; **2a**: 1.8 ± 0.1; **3a**: 1.2 ± 0.1). The results indicate that **1a**–**3a** can impair mitochondrial integrity.

Elevation of intracellular ROS levels

Mitochondria are major sites of cellular ROS production, and the loss of MMP may lead to an increase in cellular ROS.[30] The effect of Ir^{III} complexes on intracellular ROS levels was detected by flow cytometry with 2′,7′-dichlorodihydrofluorescein diacetate (H_2DCFDA) staining. The nonfluorescent H_2DCFDA can be oxidized to the highly bright 2′,7′-dichlorofluorescein (DCF) by cellular ROS.[31] As shown in Figure 6, treatment of HeLa cells with **1a**–**3a** increases the DCF fluorescence signals in a dose-dependent manner. Compared with the control, for cells treated with **1a**–**3a** (6 μM) at concentrations of approximately ten times the IC_{50} values for 6 h, the mean fluorescence intensity (MFI) increases about 5.6-, 4.5-, 5.1-fold for **1a**, **2a**, and **3a**, respectively. The results indicate that **1a**–**3a** can significantly induce elevation of intracellular ROS levels. Additionally, pretreatment of cells with *N*-acetylcysteine (NAC, an ROS scavenger) remarkably reduces the cytotoxicity of **1a**–**3a** (Figure S25 of the Supporting Information). These results suggest that ROS play a vital role in Ir^{III}-induced cell death.

Cell-cycle arrest

Cell cycle is tightly correlated with the proliferation and development of cancer cells. The cytotoxicity of many anticancer drugs is often associated with genomic DNA damage and cell-cycle perturbation.[32] It has been reported that VPA mainly induces G0/G1 cell-cycle arrest in many tumor types.[33] The effects of **1a**–**3a** on cell-cycle progression in HeLa cells were investigated. As shown in Figure S26 of the Supporting Information, on treatment of HeLa cells with **1a**–**3a** at different concentrations for 24 h, cell population in the G2/M phase was significantly increased, along with a concomitant decrease in the fraction of G0/G1 and S cells (Table S5 of the Supporting Information). The cell cycle is regulated by highly complicated molecular machinery.[34] The perturbations of cell-cycle progression induced by **1a**–**3a** and VPA are different, which indicates

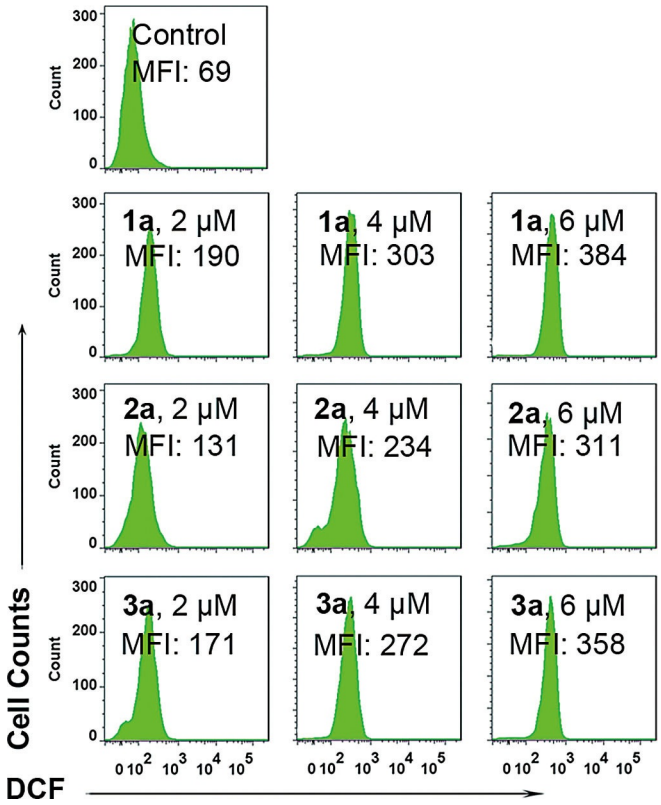

Figure 6. Effects of **1a**–**3a** on ROS generation. HeLa cells were treated with **1a**–**3a** at the indicated concentrations for 6 h, after which they were labeled with H_2DCFDA and analyzed by flow cytometry (reflected by MFI of DCF; excitation at 488 nm and emission at 525(±20) nm).

the impact of VPA on cell-cycle distribution of the conjugates is negligible.

Induction of apoptosis

Apoptosis is one of the extensively studied types of cell death, and the contribution of apoptosis to the pathogenesis of cancer has been well documented.[35] It has been reported that both iridium(III) complexes[36] and VPA[28] can induce apoptotic cell death. To investigate the mechanisms of **1a**–**3a**-induced cell death, the morphological changes of HeLa cells caused by **1a**–**3a** were examined by 2′-(4-ethoxyphenyl)-5-(4-methyl-1-piperazinyl)-1H,3′H-2,5′-bibenzimidazole (Hoechst 33342) staining. As shown in Figure 7A, vehicle-treated control cells show a normal overall morphology and a homogeneous nuclear staining pattern. After being treated with **1a**–**3a** (1 μM) at concentrations of approximately twice the IC_{50} values for 24 h, cells display morphological changes typical of apoptosis, including cell shrinkage, membrane blebbing, bright staining, chromatin condensation, nuclei fragmentation, and the presence of apoptotic bodies.[37]

Annexin V/propidium iodide (PI) dual staining can differentiate early apoptotic (annexin V-positive and PI-negative), late apoptotic and necrotic (annexin V-positive and PI-positive), and viable (annexin V-negative and PI-negative) cells. Flow-cytometric analysis showed that treatment of HeLa cells with **1a**–**3a** leads to a dose-dependent increase in the percentage of apoptotic cells. As shown in Figure 7B, after HeLa cells are treated with **1a**–**3a** (2 μM) at concentrations of approximately four times the IC_{50} values for 24 h, the percentages of cells in apoptotic phase (annexin V-positive) are 2.5, 78, 70.9, and 73.5% for control, **1a**, **2a**, and **3a**, respectively. The apoptosis-inducing capabilities of **1b**–**3b** under the same conditions were also investigated (Figure S27 of the Supporting Information). After HeLa cells were treated with **1a**–**3a** and **1b**–**3b** at concentrations on the same magnitude as the IC_{50} value, the percentages of **1a**–**3a**-treated cells in apoptotic phase were much higher than those of **1b**–**3b**-treated cells. This result implies that the released VPA may be involved in **1a**–**3a**-induced cell apoptosis.

To further clarify the mechanism by which the complexes induce apoptosis, the activity of caspase-3/7 was examined by using the Caspase-Glo® assay kit in HeLa cells after 6 h exposure to different concentrations of **1a**–**3a**. This caspase has been identified as a key executor of apoptosis under various stimuli.[38] As shown in Figure 7C, treatment of **1a**–**3a** markedly stimulates activation of caspase-3/7 in a dose-dependent manner. Moreover, cells pretreated with the pan caspase inhibitor z-VAD-FMK (50 μM) show a marked increase in cell viability compared with cells treated with Ir^{III} complexes alone (Figure 7D). These results collectively suggest that cell death induced by **1a**–**3a** mainly occurs through the caspase-dependent apoptotic pathway.

Conclusions

Three VPA-functionalized cyclometalated Ir^{III} complexes **1a**–**3a** were synthesized and characterized. All of them display excellent two-photon properties. Fluorescent spectroscopy and ESI-MS studies demonstrate that **1a**–**3a** can be quickly hydrolyzed on treatment with esterase. In vitro HDAC activity assay showed that conjugates **1a**–**3a** show similar inhibition of HDAC activity to VPA once hydrolyzed by esterase. Conjugation of the VPA to the Ir^{III} complexes can improve the lipophilicity and cellular uptake efficacy of conjugates **1a**–**3a**, and further enhances their anticancer potency. Complexes **1a**–**3a** show much higher antiproliferative activities than cisplatin against various cancer cells, especially cisplatin-resistant A549 cells, which indicates that they can overcome cisplatin resistance. Owing to their high lipophilicity and electropositivity, **1a**–**3a** can be effectively taken into HeLa cells and specifically localized to mitochondria. Further anticancer mechanistic studies indicate that these complexes can induce a series of events associated with mitochondrial damage in HeLa cells including MMP depolarization, ROS production, cell-cycle arrest, caspase activation, and apoptosis. Our study demonstrates that multifunctional anticancer drug may be achieved by conjugating metal complexes with other organic drugs through ester linkages, and the resulting conjugates provide a new strategy to build potential anticancer agents for future cancer therapy.

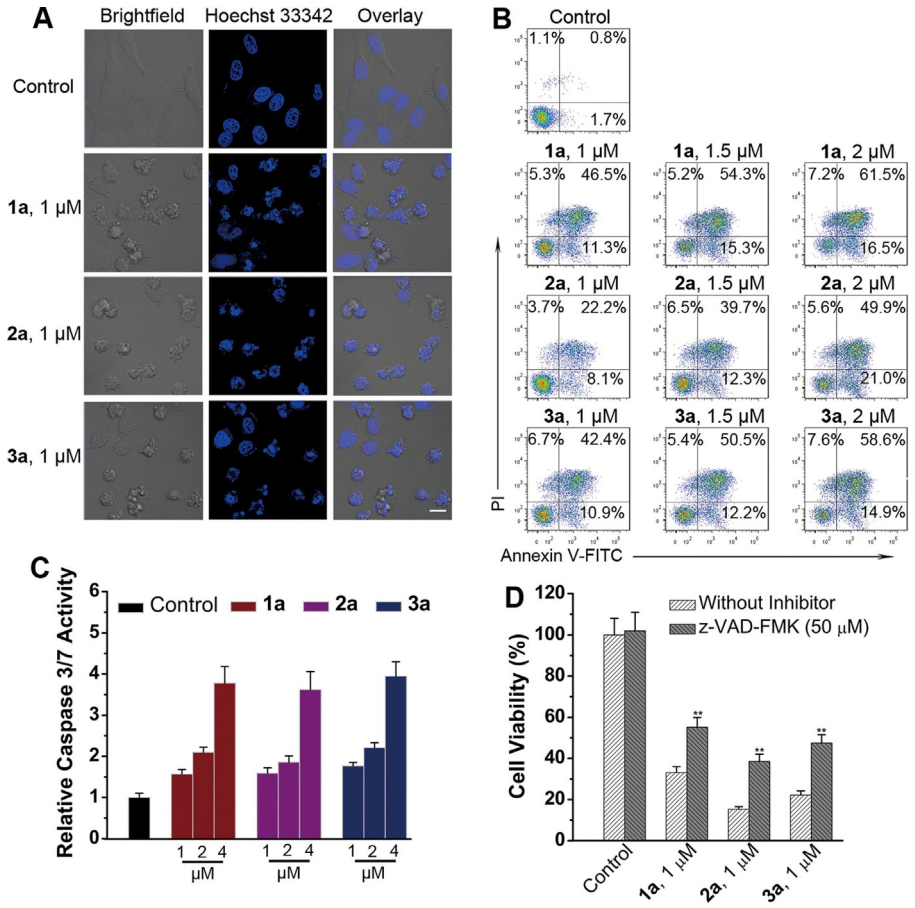

Figure 7. A) Hoechst 33342-stained HeLa cells after incubation with **1a**–**3a** for 24 h. B) Flow-cytometric quantification of annexin V and PI double-labeled HeLa cells after treatment with **1a**–**3a** for 24 h at the indicated concentrations. C) Activation of caspase-3/7 in HeLa cells treated with **1a**–**3a** at the indicated concentrations for 6 h. D) The impact of z-VAD-FMK on the cytotoxicity of **1a**–**3a**. HeLa cells were treated with **1a**–**3a** for 48 h at the indicated concentrations in the absence or presence of z-VAD-FMK. Cell viability was measured by MTT assay. Data are represented as mean ± SD of three independent experiments. $^{**}p < 0.005$, compared with the cell viability of Ir^{III} treatment alone.

Experimental Section

General materials and methods

Iridium chloride hydrate, 2-phenylpyridine (ppy), 2-(2,4-difluorophenyl)pyridine (dfppy), 2-(2-thienyl)pyridine (thpy), HMbpy, 2-propylvaleryl chloride, and NH_4PF_6 were purchased from Alfa Aesar. Cisplatin, DMSO, PLE [$(NH_4)_2SO_4$ suspension, $\geq$150 units mg^{-1} protein], VPA, CCCP, chloroquine, MTT, JC-1, H_2DCFDA, NAC, PI, Annexin V-FITC apoptosis detection kit, Hoechst 33342, and z-VAD-fmk were purchased from Sigma-Aldrich. The fluorescent HDAC activity assay kit was purchased from Enzo Life Sciences (USA). MTDR and LTDR were purchased from Life Technologies (USA). Caspase-3/7 activity assay kit was purchased from Promega (USA).

The cyclometalated Ir^{III} chlorido-bridged dimers $[\{Ir(ppy)_2Cl\}_2]$,[39] $[\{Ir(dfppy)_2Cl\}_2]$[40] and $[\{Ir(thpy)_2Cl\}_2]$[41] were prepared according to literature methods. The purity of the synthesized compounds was analyzed by combustion analysis and they were found to be $\geq$95% pure. All the tested compounds were dissolved in DMSO just before the experiments, and the concentration of DMSO was 1 vol% in PBS. The solutions of **1a**–**3a** and **1b**–**3b** in PBS proved to be stable for at least 48 h at room temperature, as monitored by UV/Vis spectroscopy.

General instrumentation

ESI-MS, microanalysis (C, H, N), and ^{1}H NMR and ^{13}C NMR measurements were performed with an LCQ DECA XP spectrometer (USA), an Elementar Vario EL CHNS analyzer (Germany), and a Bruker Avance 400 spectrometer (Germany), respectively. The XRD pattern was collected with a Bruker D8 Advance diffractometer. UV/Vis spectra emission spectra and time-resolved emission data were recorded with a Varian Cary 300 spectrophotometer (USA) and an FLS 920 combined fluorescence lifetime and steady-state spectrometer (Japan), respectively. The two-photon fluorescence data were acquired with an Opolette™ 355II (pulse width $\leq$100 fs, 80 MHz repetition rate, tuning range 720–890 nm, Spectra Physics Inc., USA). Ir content was measured with a Thermo X Series 2 ICP-MS (USA). The cell viability and HDAC inhibition activity were determined with a TECAN Infinite M200 Pro microplate reader (Switzerland). Confocal microscopy images were obtained with a LSM 710 confocal laser scanning fluorescence microscope (Carl Zeiss, Germany). Flow-cytometric analysis was performed with a BD FACS Calibur™ flow cytometer (Becton Dickinson, USA).

General synthetic procedures for ligand L and iridium(III) complexes

Ligand L: As shown in Scheme S1 of the Supporting Information, HMbpy (2.5 mmol) and Et_3N (15 mmol) were dissolved in dry DMF

(45 mL), and 2-propylvaleryl chloride (2.5 mmol) in dry DMF was then added dropwise. The mixture was stirred under nitrogen for 12 h at room temperature, and then concentrated to give yellow oily liquid, which was used directly for the next step without further purification.

Complexes 1a–3a. As shown in Scheme S2 of the Supporting Information, **1a–3a** were synthesized by heating ligand **L** (0.46 mmol, 2 equiv) and the appropriate iridium(III) chloride-bridged dimer (0.23 mmol, 1 equiv) in refluxing CH_2Cl_2/CH_3OH (2:1 v/v), followed by anion exchange with saturated NH_4PF_6 solution and purification by recrystallization from CH_2Cl_2/diethyl ether.

Complexes 1b–3b: Complexes **1b–3b** were synthesized according to the synthetic procedure for **1a–3a**, with slight modification, by using HMbpy instead of ligand **L**.

[Ir(ppy)$_2$(L)](PF$_6$) (1a): Complex **1a** was synthesized according to the synthetic procedure described above, which gave the product as an orange powder. Yield: 0.353 g (79%). ^{1}H NMR (400 MHz, [D$_6$]DMSO): δ = 8.84 (d, J = 4.0 Hz, 1H), 8.72 (d, J = 4.1 Hz, 1H), 8.28 (d, J = 7.1 Hz, 2H), 7.93 (d, J = 6.5 Hz, 4H), 7.88 (d, J = 5.6 Hz, 1H), 7.73–7.61 (m, 4H), 7.56 (d, J = 5.2 Hz, 1H), 7.20–7.13 (m, 2H), 7.06–6.98 (m, 2H), 6.95–6.87 (m, 2H), 6.27–6.16 (m, 2H), 5.33 (d, J = 4.9 Hz, 2H), 2.55 (d, J = 5.3 Hz, 3H), 1.49 (m, 4H), 1.26–1.15 (m, 4H), 1.09 (d, J = 6.9 Hz, 1H), 0.86–0.76 ppm (m, 6H); ^{13}C NMR (100 MHz, [D$_6$]DMSO): δ = 175.49, 167.35, 155.93, 155.16, 152.05, 150.90, 150.43, 149.66, 149.41, 144.23, 139.20, 131.57, 130.69, 129.89, 126.91, 126.08, 125.52, 124.33, 123.48, 122.70, 120.48, 63.70, 44.66, 34.30, 21.40, 20.42, 14.24 ppm; ESI-MS (CH_2Cl_2): m/z 827.55 [M−PF$_6$]$^+$; elemental analysis calcd (%) for $C_{42}H_{42}F_6IrN_4O_2P\cdot 3H_2O$: C 49.16, H 4.72, N 5.46; found: C 49.39, H 4.39, N 5.77.

[Ir(dfppy)$_2$(L)](PF$_6$) (2a): Complex **2a** was synthesized according to the synthetic procedure described above, which gave the product as a bright yellow powder. Yield: 0.393 g (82%). ^{1}H NMR (400 MHz, [D$_6$]DMSO): δ = 8.85 (s, 1H), 8.74 (s, 1H), 8.30 (d, J = 8.3 Hz, 2H), 8.04 (t, J = 7.7 Hz, 2H), 7.94 (d, J = 5.7 Hz, 1H), 7.78–7.66 (m, 4H), 7.57 (d, J = 5.5 Hz, 1H), 7.28–7.22 (m, 2H), 6.97 (t, J = 10.9 Hz, 2H), 5.63 (t, J = 6.9 Hz, 2H), 5.35 (s, 2H), 2.57 (s, 3H), 1.61–1.38 (m, 4H), 1.21 (dd, J = 14.6, 7.3 Hz, 4H), 1.09 (t, J = 7.0 Hz, 1H), 0.82 ppm (td, J = 7.2, 4.0 Hz, 6H); ^{13}C NMR (100 MHz, [D$_6$]DMSO): δ = 175.47, 163.30, 155.33, 152.69, 150.93, 150.24, 149.97, 140.47, 130.27, 128.06, 127.13, 126.31, 124.93, 123.72, 113.65, 99.46, 63.66, 44.69, 34.30, 21.44, 20.43, 14.23 ppm; ESI-MS (CH_2Cl_2): m/z 899.65 [M-PF$_6$]$^+$; elemental analysis calcd (%) for $C_{42}H_{38}F_{10}IrN_4O_2P\cdot H_2O$: C 47.50, H 3.80, N 5.28; found: C 47.25, H 3.63, N 5.47.

[Ir(thpy)$_2$(L)](PF$_6$) (3a): Complex **3a** was synthesized according to the synthetic procedure described above, which gave the product as a brown powder. Yield: 0.384 g (85%). ^{1}H NMR (400 MHz, [D$_6$]DMSO): δ = 8.82 (s, 1H), 8.71 (s, 1H), 7.80 (m, 5H), 7.71–7.64 (m, 4H), 7.59 (d, J = 5.5 Hz, 1H), 7.53 (t, J = 4.9 Hz, 2H), 6.96 (dd, J = 9.1, 5.6 Hz, 2H), 6.18 (t, J = 4.9 Hz, 2H), 5.34 (s, 2H), 2.56 (s, 3H), 1.60–1.40 (m, 4H), 1.21 (dd, J = 14.7, 7.3 Hz, 4H), 1.10 (t, J = 7.0 Hz, 1H), 0.82 ppm (td, J = 7.2, 3.6 Hz, 6H); ^{13}C NMR (100 MHz, [D$_6$]DMSO): δ = 175.49, 163.44, 156.07, 155.29, 152.83, 152.19, 151.05, 150.17, 149.74, 139.77, 136.64, 131.34, 130.76, 130.02, 127.02, 126.02, 123.40, 121.38, 118.73, 63.69, 44.67, 34.30, 21.40, 20.43, 14.24 ppm; ESI-MS (CH_2Cl_2): m/z 839.40 [M−PF$_6$]$^+$; elemental analysis calcd (%) for $C_{38}H_{38}F_6IrN_4O_2PS_2\cdot H_2O$: C 45.55, H 4.02, N 5.59; found: C 45.41, H 3.90, N 5.62.

[Ir(ppy)$_2$(HMbpy)](PF$_6$) (1b): Complex **1b** was synthesized according to the synthetic procedure described above, which gave the product as an orange powder. Yield: 0.330 g (85%). ^{1}H NMR (400 MHz, [D$_6$]DMSO): δ = 8.76 (d, J = 7.1 Hz, 2H), 8.27 (d, J = 8.1 Hz, 2H), 7.93 (t, J = 8.7 Hz, 4H), 7.80 (d, J = 5.6 Hz, 1H), 7.70 (d, J = 5.6 Hz, 1H), 7.66–7.60 (m, 3H), 7.52 (d, J = 5.4 Hz, 1H), 7.17 (t, J = 6.5 Hz, 2H), 7.02 (t, J = 7.4 Hz, 2H), 6.90 (t, J = 7.3 Hz, 2H), 6.21 (d, J = 7.1 Hz, 2H), 5.76 (s, 1H), 4.75 (s, 2H), 2.54 ppm (s, 3H); ^{13}C NMR (100 MHz, [D$_6$]DMSO): δ = 167.36, 156.33, 155.52, 152.06, 151.15, 149.82, 149.48, 149.19, 144.28, 139.13, 131.57, 130.66, 129.69, 126.04, 125.50, 124.31, 122.62, 122.22, 120.44, 61.83, 21.31 ppm; ESI-MS (CH_2Cl_2): m/z 701.25 [M−PF$_6$]$^+$; elemental analysis calcd (%) for $C_{34}H_{28}F_6IrN_4OP\cdot 0.4(C_2H_5)_2O$: C 48.84, H 3.68, N 6.40; found: C 48.55, H 3.88, N 6.25.

[Ir(dfppy)$_2$(HMbpy)](PF$_6$) (2b): Complex **2b** was synthesized according to the synthetic procedure described above, which gave the product as a bright yellow powder. Yield: 0.337 g (80%). ^{1}H NMR (400 MHz, [D$_6$]DMSO): δ = 8.78 (d, J = 11.0 Hz, 2H), 8.30 (d, J = 8.4 Hz, 2H), 8.04 (t, J = 7.8 Hz, 2H), 7.86 (d, J = 5.6 Hz, 1H), 7.76 (d, J = 5.6 Hz, 1H), 7.71 (t, J = 5.0 Hz, 2H), 7.65 (d, J = 5.5 Hz, 1H), 7.55 (d, J = 5.4 Hz, 1H), 7.26 (t, J = 6.6 Hz, 2H), 6.97 (t, J = 10.6 Hz, 2H), 5.76 (s, 1H), 5.64 (d, J = 7.9 Hz, 2H), 4.77 (d, J = 5.3 Hz, 2H), 2.56 ppm (s, 3H); ^{13}C NMR (100 MHz, [D$_6$]DMSO): δ = 163.26, 156.94, 155.32, 152.71, 150.27, 149.91, 140.41, 130.07, 128.05, 126.35, 124.93, 123.79, 122.42, 113.71, 61.80, 21.35 ppm; ESI-MS (CH_2Cl_2): m/z 773.35 [M−PF$_6$]$^+$; elemental analysis calcd (%) for $C_{34}H_{24}F_{10}IrN_4OP\cdot 2H_2O$: C 42.82, H 2.96, N 5.87; found: C 42.68, H 2.87, N 5.76.

[Ir(thpy)$_2$(HMbpy)](PF$_6$) (3b): Complex **3b** was synthesized according to the synthetic procedure described above, which gave the product as a brown powder. Yield: 0.319 g (81%). ^{1}H NMR (400 MHz, [D$_6$]DMSO): δ = 8.74 (d, J = 5.9 Hz, 2H), 7.81 (t, J = 7.7 Hz, 2H), 7.76 (t, J = 6.6 Hz, 3H), 7.65 (dd, J = 9.0, 5.1 Hz, 4H), 7.57–7.51 (m, 3H), 6.96 (t, J = 6.5 Hz, 2H), 6.19 (dd, J = 4.7, 1.9 Hz, 2H), 5.75 (s, 1H), 4.76 (s, 2H), 2.55 ppm (s, 3H); ^{13}C NMR (100 MHz, [D$_6$]DMSO): δ = 163.49, 156.46, 155.66, 153.11, 152.21, 150.42, 150.06, 149.70, 139.70, 136.57, 131.29, 130.82, 129.82, 126.22, 126.08, 122.15, 121.39, 118.69, 61.81, 21.31 ppm; ESI-MS (CH_2Cl_2): m/z 713.25 [M−PF$_6$]$^+$; elemental analysis calcd (%) for $C_{30}H_{24}F_6IrN_4OPS_2\cdot 1.5H_2O$: C 40.72, H 3.08, N 6.33; found: C 40.99, H 3.05, N 6.07.

Crystallographic structure determination

Crystals of **2a** and **2b** suitable for X-ray analysis were obtained by slow diffusion of diethyl ether in to CH_2Cl_2 solutions. The crystal structures of **2a** and **2b** were solved by direct methods with SHELXS and refined by the full-matrix least-squares technique with SHELXL.[42] Crystal data and selected bond lengths and angles are listed in Tables S1 and S2 of the Supporting Information.

Determination of TPA cross sections

The TPA spectra were determined at 720–890 nm by the typical two-photon laser-induced fluorescence method.[43] Two-photon fluorescence measurements were performed in fluorometric quartz cuvettes with Ir^{III} complexes (5×10^{-4} M) in CH_3OH at 298 K by using rhodamine B (5×10^{-5} M) as reference. The TPA cross section was calculated according to Equation (1):[44]

$$\delta_s = \delta_r \frac{\Phi_r c_r I_s n_s}{\Phi_s c_s I_r n_r} \quad (1)$$

where δ is the TPA cross section, Φ the quantum yield, c the concentration, I the integrated fluorescence intensity, and n the refractive index. Subscript r stands for reference, and s for sample.

Hydrolysis of 1a–3a by PLE in vitro

Time-dependent emission spectra: Mixtures of **1a–3a** (2×10^{-5} M) with degassed PBS were freshly prepared in quartz cuvettes (3 mL), and then a suspension of PLE (1 μL) in $(NH_4)_2SO_4$ was added. Time-dependent emission spectra were recorded after reaction for 5 min at 298 K.

Luminescence decay signals: Mixtures of **1a–3a** (2×10^{-5} M) with degassed PBS were freshly prepared in quartz cuvettes (3 mL), and then a suspension of PLE (1 μL) in $(NH_4)_2SO_4$ was added. After the mixtures were incubated at 298 K for the indicated time intervals, luminescence decay curves were recorded.

ESI-MS: Complexes **1a–3a** (2×10^{-5} M) were dissolved in freshly prepared PBS buffer (3 mL), and then a suspension of PLE (1 μL) in $(NH_4)_2SO_4$ was added. After the mixtures were incubated at 298 K for the indicated time intervals, acetone (400 μL, 253 K) was added to quench the enzymatic hydrolysis. The samples were centrifuged (15000 *g*, 10 min). The supernatant was collected and analyzed by ESI-MS.

HDAC enzyme inhibition assay

The ability of the compounds to inhibit HDACs was investigated in triplicate by following the experimental procedure supplied with the assay kit. First, the master mixture was prepared from the HDAC substrate solution (25 μL/well) and HDAC assay buffer (25 μL/well). The master mixture was pipetted to all wells (50 μL/well). After that, 1 mM solutions of tested inhibitors (VPA, **1a–3a**, and **1b–3b**), which were prepared in water from their stock solutions in DMSO, were added to the plate (10 μL/well). For the inhibition activity in the presence of the esterase, **1a–3a** (1 mM) were pretreated with PLE (1 μL) at 298 K for 10 h, and then directly added to the corresponding wells (10 μL/well). The plates were incubated at 37 °C for 30 min. HDAC developer (50 μL/well) was pipetted into all wells and the plates were incubated at room temperature for an additional 30 min. The fluorescence was detected at excitation/emission wavelengths of 340 and 460 nm by using a fluorescence microplate reader. IC_{50} values (the drug concentration required to inhibit HDAC activity by 50%) were calculated according to a regression analysis of the concentration/inhibition data.

Determination of lipophilicity

The lg*P* values were determined by the flask-shaking method. Briefly, equal amounts of aqueous sodium chloride (0.9 wt%) and *n*-octanol were mutually saturated for one week, and then the mixture was separated to obtain oil and aqueous phases. Complexes **1a–3a** and **1b–3b** were dissolved in the aqueous phase, and an equal volume of the saturated *n*-octanol was added. The solutions were shaken in the oscillator for 24 h, and then centrifuged at 1500 *g* for 10 min. The Ir^{III} content of the *n*-octanol and aqueous phases was determined by UV/Vis spectroscopy, and lg*P* was calculated as the logarithmic ratio of Ir^{III} concentration in *n*-octanol to that in the aqueous phases.

ICP-MS measurement

Cellular accumulation of Ir^{III} complexes was determined in HeLa cells. Cells were seeded in 10 cm tissue culture dishes and incubated for 24 h. The medium was removed and replaced with fresh medium containing the tested Ir^{III} complexes (5 μM). After 30 min incubation, the cells were collected, counted, and then digested with HNO_3 (65%, 0.2 mL) at room temperature for at least 24 h. The quantity of Ir taken up by HeLa cells was determined by ICP-MS.

Cytotoxicity assay

The growth inhibitory effect of the tested compounds towards HeLa, A549, A549R, HepG2 and LO2 cells lines was evaluated by MTT assay as previously described.[27] For the cytotoxicity assay in the presence of the inhibitors (*z*-VAD-FMK or NAC), HeLa cells were preincubated with inhibitors at the indicated concentrations for 1 h before the complexes were added.

One- and two-photon cellular imaging

HeLa cells were co-incubated with Ir^{III} complexes (5 μM) and MTDR (150 nM) or LTDR (50 nM) at 37 °C for 30 min. Cells were washed three times with PBS and visualized by confocal microscopy immediately; $\lambda_{ex}=405$ (OPM) or 740 nm (TPM) for Ir^{III} complexes and 633 nm for MTDR and LTDR; $\lambda_{em}=600(\pm20)$ nm for **1a**, 530(±20) nm for **2a**, 630(±20) nm for **3a**, 665(±20) nm for MTDR, and 668(±20) nm for LTDR, respectively.

Cellular uptake mechanism studies

To investigate the impact of temperature and metabolic or endocytic inhibitors on cellular uptake of **1a–3a**, HeLa cells were seeded in 35 mm dishes and cultured for 24 h. For temperature tests, cells were incubated with Ir^{III} complexes (5 μM) at 4 and 37 °C for 30 min; for inhibitor tests, cells were pretreated with 30 μM CCCP or 50 μM chloroquine for 1 h at 37 °C and then incubated with Ir^{III} complexes (5 μM) at 37 °C for a further 30 min. In each case, cells were washed three times with PBS and visualized by confocal microscopy; $\lambda_{ex}=405$ nm (OPM) or 740 nm (TPM); $\lambda_{em}=600(\pm20)$ nm for **1a**, 530(±20) nm for **2a**, and 630(±20) nm for **3a**.

Analysis of MMP

The impact of **1a–3a** on MMP was determined as previously described.[27] Briefly, HeLa cells were treated with **1a–3a** at the indicated concentrations for 6 h, collected, and stained with 5 μg mL^{-1} JC-1. The fluorescence intensity of the cells was measured immediately by flow cytometry with excitation at 488 nm and dual emission at 530 (green) and 590 nm (red). MFI was analyzed with FlowJo 7.6 software.

Measurement of intracellular ROS

The impact of **1a–3a** on ROS levels was determined as previously described.[27] Briefly, HeLa cells were treated with **1a–3a** at the indicated concentrations for 6 h, collected, and incubated with 10 μM H_2DCFDA in serum-free Dulbecco's modified Eagle's medium (DMEM) for 15 min at 37 °C. The fluorescence intensity of the cells was measured by flow cytometry with excitation at 488 nm and emission at 530 nm. Green MFI was analyzed with FlowJo 7.6 software.

Cell-cycle analysis

The impact of the tested complexes on cell-cycle distribution was analyzed by flow cytometry and PI staining as previously described.[12a]

Detection of apoptosis

Hoechst staining: HeLa cells were seeded into 35 mm dishes and treated with **1a**–**3a** for 24 h. The cells were then washed once with PBS and fixed with 4% paraformaldehyde at room temperature for 10 min. Then, cells were labeled with Hoechst 33342 (5 $\mu g\,mL^{-1}$ in PBS) for 5 min. The cells were analyzed immediately with a confocal microscope.

Annexin V/PI assay: For apoptosis determination assays, HeLa cells were cultured in six-well plates and incubated with the indicated concentrations of Ir^{III} complexes for 24 h. After treatment, cells were harvested and stained with 5 μL annexin V and 10 μL PI at room temperature for 10 min in the dark, and analyzed immediately by flow cytometry with excitation at 488 nm. Data were analyzed with FlowJo 7.6 software.

Caspase-3/7 activity assay: Activation of Caspase-3/7 by **1a**–**3a** was measured by using the Caspase-Glo® Assay kit according to the manufacturer's instructions with a slight modification. Briefly, HeLa cells were cultured in 48-well plates and treated with different concentration of Ir^{III} complexes for 6 h. Cells were washed three times with PBS and then lysed. 50 μL cell lysate was added to each well, followed by the addition of 50 μL Caspase-Glo® 3/7 reagent. The mixture was incubated at room temperature for 30 min and then the luminescence was measured with a TECAN Infinite M200 station. Cells treated with vehicle control DMSO (1%, v/v) were used as the reference group.

Statistical analysis

All biological experiments were performed at least twice in triplicate in each experiment. Representative results are depicted in this report and data were presented as mean ± SD.

Acknowledgements

This study was supported by the National Natural Science Foundation of China (Nos. 21231007, 21572282 and 21571196), the 973 program (Nos. 2014CB845604 and 2015CB856301), the Guangdong Natural Science Foundation (2015A030306023), China Postdoctoral Science Foundation (2016M590832) and the Fundamental Research Funds for the Central Universities.

Conflict of interest

The authors declare no conflict of interest.

Keywords: antitumor agents · apoptosis · imaging agents · iridium · N ligands

[1] a) Z. Liu, P. J. Sadler, *Acc. Chem. Res.* **2014**, *47*, 1174 – 1185; b) A. Wilbuer, D. H. Vlecken, D. J. Schmitz, K. Kraling, K. Harms, C. P. Bagowski, E. Meggers, *Angew. Chem. Int. Ed.* **2010**, *49*, 3839 – 3842; *Angew. Chem.* **2010**, *122*, 3928 – 3932.

[2] a) D.-L. Ma, S. Lin, W. Wang, C. Yang, C.-H. Leung, *Chem. Sci.* **2017**, *8*, 878 – 889; b) Y. Chen, R. L. Guan, C. Zhang, J. J. Huang, L. N. Ji, H. Chao, *Coord. Chem. Rev.* **2016**, *310*, 16 – 40.

[3] a) M. H. Chen, F. X. Wang, J. J. Cao, C. P. Tan, L. N. Ji, Z. W. Mao, *ACS Appl. Mater. Interfaces* **2017**, *9*, 13304 – 13314; b) K. Qiu, H. Huang, B. Liu, Y. Liu, Z. Huang, Y. Chen, L. Ji, H. Chao, *ACS Appl. Mater. Interfaces* **2016**, *8*, 12702 – 12710; c) J. S. Nam, M.-G. Kang, J. Kang, S.-Y. Park, S. J. C. Lee, H.-T. Kim, J. K. Seo, O.-H. Kwon, M. H. Lim, H.-W. Rhee, T.-H. Kwon, *J. Am. Chem. Soc.* **2016**, *138*, 10968 – 10977; d) W. Lv, Z. Zhang, K. Y. Zhang, H. Yang, S. Liu, A. Xu, S. Guo, Q. Zhao, W. Huang, *Angew. Chem. Int. Ed.* **2016**, *55*, 9947 – 9951; *Angew. Chem.* **2016**, *128*, 10101 – 10105; e) R. R. Ye, C. P. Tan, L. N. Ji, Z. W. Mao, *Dalton Trans.* **2016**, *45*, 13042 – 13051; f) L. He, C.-P. Tan, R.-R. Ye, Y.-Z. Zhao, Y.-H. Liu, Q. Zhao, L.-N. Ji, Z.-W. Mao, *Angew. Chem. Int. Ed.* **2014**, *53*, 12137 – 12141; *Angew. Chem.* **2014**, *126*, 12333 – 12337.

[4] a) L.-J. Liu, L. Lu, H.-J. Zhong, B. He, D. W. J. Kwong, D.-L. Ma, C.-H. Leung, *J. Med. Chem.* **2015**, *58*, 6697 – 6703; b) C.-H. Leung, H.-J. Zhong, H. Yang, Z. Cheng, D. S.-H. Chan, V. P.-Y. Ma, R. Abagyan, C.-Y. Wong, D.-L. Ma, *Angew. Chem. Int. Ed.* **2012**, *51*, 9010 – 9014; *Angew. Chem.* **2012**, *124*, 9144 – 9148; c) R.-R. Ye, C.-P. Tan, L. He, M.-H. Chen, L.-N. Ji, Z.-W. Mao, *Chem. Commun.* **2014**, *50*, 10945 – 10948.

[5] a) L. He, Y. Li, C.-P. Tan, R.-R. Ye, M.-H. Chen, J.-J. Cao, L.-N. Ji, Z.-W. Mao, *Chem. Sci.* **2015**, *6*, 5409 – 5418; b) X. Tian, Y. Zhu, M. Zhang, L. Luo, J. Wu, H. Zhou, L. Guan, G. Battaglia, Y. Tian, *Chem. Commun.* **2017**, *53*, 3303 – 3306; c) L. K. McKenzie, I. V. Sazanovich, E. Baggaley, M. Bonneau, V. Guerchais, J. A. G. Williams, J. A. Weinstein, H. E. Bryant, *Chem. Eur. J.* **2017**, *23*, 234 – 238.

[6] a) J. J. Cao, C. P. Tan, M. H. Chen, N. Wu, D. Y. Yao, X. G. Liu, L. N. Ji, Z. W. Mao, *Chem. Sci.* **2017**, *8*, 631 – 640; b) Y. Li, C.-P. Tan, W. Zhang, L. He, L.-N. Ji, Z.-W. Mao, *Biomaterials* **2015**, *39*, 95 – 104.

[7] S. Fulda, L. Galluzzi, G. Kroemer, *Nat. Rev. Drug Discovery* **2010**, *9*, 447 – 464.

[8] A. H. V. Schapira, *Lancet* **2012**, *379*, 1825 – 1834.

[9] S. E. Weinberg, N. S. Chandel, *Nat. Chem. Biol.* **2015**, *11*, 9 – 15.

[10] J. E. Bolden, M. J. Peart, R. W. Johnstone, *Nat. Rev. Drug Discovery* **2006**, *5*, 769 – 784.

[11] B. S. Mann, J. R. Johnson, M. H. Cohen, R. Justice, R. Pazdur, *Oncologist* **2007**, *12*, 1247 – 1252.

[12] a) R.-R. Ye, Z.-F. Ke, C.-P. Tan, L. He, L.-N. Ji, Z.-W. Mao, *Chem. Eur. J.* **2013**, *19*, 10160 – 10169; b) R.-R. Ye, C.-P. Tan, Y.-N. Lin, L.-N. Ji, Z.-W. Mao, *Chem. Commun.* **2015**, *51*, 8353 – 8356.

[13] W. Löscher, *CNS Drugs* **2002**, *16*, 669 – 694.

[14] D. C. Drummond, C. O. Noble, D. B. Kirpotin, Z. X. Guo, G. K. Scott, C. C. Benz, *Annu. Rev. Pharmacol. Toxicol.* **2005**, *45*, 495 – 528.

[15] N. Gurvich, O. M. Tsygankova, J. L. Meinkoth, P. S. Kein, *Cancer Res.* **2004**, *64*, 1079 – 1086.

[16] J. Yang, X. R. Sun, W. W. Mao, M. H. Sui, J. B. Tang, Y. Q. Shen, *Mol. Pharm.* **2012**, *9*, 2793 – 2800.

[17] M. Alessio, I. Zanellato, I. Bonarrigo, E. Gabano, M. Ravera, D. Osella, *J. Inorg. Biochem.* **2013**, *129*, 52 – 57.

[18] V. Novohradsky, L. Zerzankova, J. Stepankova, O. Vrana, R. Raveendran, D. Gibson, J. Kasparkova, V. Brabec, *Biochem. Pharmacol.* **2015**, *95*, 133 – 144.

[19] R. Raveendran, J. P. Braude, E. Wexselblatt, V. Novohradsky, O. Stuchlikova, V. Brabec, V. Gandin, D. Gibson, *Chem. Sci.* **2016**, *7*, 2381 – 2391.

[20] R. Humerickhouse, K. Lohrbach, L. Li, W. F. Bosron, M. E. Dolan, *Cancer Res.* **2000**, *60*, 1189 – 1192.

[21] a) Q. Zhao, S. Liu, M. Shi, C. Wang, M. Yu, L. Li, F. Li, T. Yi, C. Huang, *Inorg. Chem.* **2006**, *45*, 6152 – 6160; b) R. Liu, N. Dandu, J. Chen, Y. Li, Z. Li, S. Liu, C. Wang, S. Kilina, B. Kohler, W. Sun, *J. Phys. Chem. C* **2014**, *118*, 23233 – 23246.

[22] W. R. Zipfel, R. M. Williams, W. W. Webb, *Nat. Biotechnol.* **2003**, *21*, 1369 – 1377.

[23] G. Li, Q. Lin, L. Sun, C. Feng, P. Zhang, B. Yu, Y. Chen, Y. Wen, H. Wang, L. Ji, H. Chao, *Biomaterials* **2015**, *53*, 285 – 295.

[24] T. Imai, *Drug Metab. Pharmacokinet.* **2006**, *21*, 173 – 185.

[25] F. C. M. Leung, A. Y. Y. Tam, V. K. M. Au, M. J. Li, V. W. W. Yam, *Acs Appl. Mater. Interfaces* **2014**, *6*, 6644 – 6653.

[26] Q. Fu, J. Tang, M. Cui, Z. Zheng, Z. Q. Liu, S. Y. Liu, *J. Chromatogr. B* **2015**, *990*, 169 – 173.

[27] R.-R. Ye, C.-P. Tan, M.-H. Chen, L. Hao, L.-N. Ji, Z.-W. Mao, *Chem. Eur. J.* **2016**, *22*, 7800 – 7809.

[28] N. Takai, N. Kawamata, D. Gui, J. W. Said, I. Miyakawa, H. P. Koeffler, *Cancer* **2004**, *101*, 2760 – 2770.

[29] S. T. Smiley, M. Reers, C. Mottola-Hartshorn, M. Lin, A. Chen, T. W. Smith, G. D. Steele, Jr., L. B. Chen, *Proc. Natl. Acad. Sci. USA* **1991**, *88*, 3671 – 3675.

[30] P. T. Schumacker, *Cancer Cell* **2006**, *10*, 175 – 176.

[31] R. Cathcart, E. Schwiers, B. N. Ames, *Anal. Biochem.* **1983**, *134*, 111 – 116.

[32] G. I. Shapiro, J. W. Harper, *J. Clin. Invest.* **1999**, *104*, 1645 – 1653.
[33] Y. W. Chou, N. K. Chaturvedi, S. G. Ouyang, F. F. Lin, D. Kaushik, J. Wan, I. Kim, M. F. Lin, *Cancer Lett.* **2011**, *311*, 177 – 186.
[34] A. W. Murray, *Cell* **2004**, *116*, 221 – 234.
[35] C. P. Tan, Y. Y. Lu, L. N. Ji, Z. W. Mao, *Metallomics* **2014**, *6*, 978 – 995.
[36] a) J. M. Hearn, I. Romero-Canelón, B. Qamar, Z. Liu, I. Hands-Portman, P. J. Sadler, *ACS Chem. Biol.* **2013**, *8*, 1335 – 1343; b) A. Kastl, A. Wilbuer, A. L. Merkel, L. Feng, P. Di Fazio, M. Ocker, E. Meggers, *Chem. Commun.* **2012**, *48*, 1863 – 1865.
[37] R. S. Hotchkiss, A. Strasser, J. E. McDunn, P. E. Swanson, *N. Engl. J. Med.* **2009**, *361*, 1570 – 1583.
[38] N. A. Thornberry, Y. Lazebnik, *Science* **1998**, *281*, 1312 – 1316.
[39] K. A. King, R. J. Watts, *J. Am. Chem. Soc.* **1987**, *109*, 1589 – 1590.
[40] Y. M. You, S. Y. Park, *J. Am. Chem. Soc.* **2005**, *127*, 12438 – 12439.
[41] C. Li, M. Yu, Y. Sun, Y. Wu, C. Huang, F. Li, *J. Am. Chem. Soc.* **2011**, *133*, 11231 – 11239.
[42] G. M. Sheldrick, *Acta Crystallogr. Sect. A* **2008**, *64*, 112 – 122.
[43] N. S. Makarov, M. Drobizhev, A. Rebane, *Opt. Express* **2008**, *16*, 4029 – 4047.
[44] C. Xu, W. W. Webb, *J. Opt. Soc. Am. B* **1996**, *13*, 481 – 491.

Manuscript received: July 8, 2017
Revised manuscript received: August 14, 2017
Accepted manuscript online: August 22, 2017
Version of record online: October 9, 2017